JACS
JOURNAL OF THE AMERICAN CHEMICAL SOCIETY

Article

pubs.acs.org/JACS

Reversible Kirkwood–Alder Transition Observed in Pt_3Cu_2 Nanoctahedron Assemblies under Controlled Solvent Annealing/Drying Conditions

Jun Zhang,[†,#] Zhiping Luo,[‡,¶] Benjamin Martens,[∥] Zewei Quan,[†] Amar Kumbhar,[§] Nathan Porter,[†] Yuxuan Wang,[∥] Detlef-M. Smilgies,*[,⊥] and Jiye Fang*[,†,∥]

[†]Department of Chemistry and [∥]Materials Science and Engineering Program, State University of New York at Binghamton, Binghamton, New York 13902, United States

[‡]Microscopy and Imaging Center and Materials Science and Engineering Program, Texas A&M University, College Station, Texas 77843, United States

[§]Chapel Hill Analytical and Nanofabrication Laboratory, University of North Carolina at Chapel Hill, Chapel Hill, North Carolina 27599, United States

[⊥]Cornell High Energy Synchrotron Source (CHESS), Cornell University, Ithaca, New York 14853, United States

Supporting Information

ABSTRACT: We report a Kirkwood–Alder transition in a system of nonspherical Pt_3Cu_2 nanoctahedra coated with oleic acid and oleylamine ligands. Using both transmission electron microscopy tomography with 3D reconstruction analysis and synchrotron-based *in-situ* grazing-incidence small-angle X-ray scattering (GISAXS) techniques, we specifically determined that these nanoctahedra can assemble into an open structure in which the nanoctahedra are arranged tip-to-tip to form a *bcc* superlattice with a low packing efficiency. Using *in-situ* and real-time GISAXS, we further observed a "nanoctahedron crystallization" as a soft Kirkwood–Alder transition, that is, the soft nanoactahedra crystallize at a critical concentration and possess continuous crystalline states during a period of solvent evaporation. Finally, we found a reversible change of the superlattice constant during the solvent annealing and evaporation/drying processes.

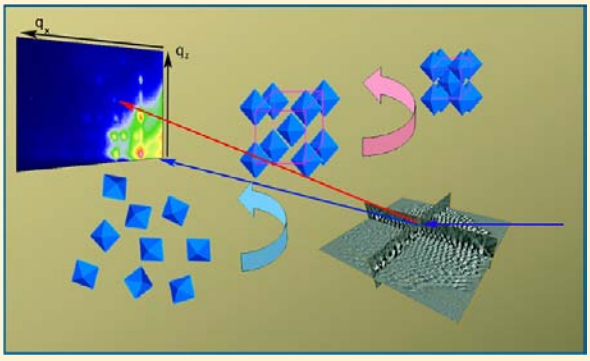

INTRODUCTION

In their classic theoretical study, Kirkwood and Alder predicted that a solution of hard spheres would undergo a phase transition to form an ordered lattice at a critical sphere concentration.[1−4] In recent years, this concept has also been extended to hold for soft spheres.[5] In this case, particles are surrounded by flexible organic ligands that prevent irreversible clumping and make particles highly solvable, for instance, colloids, block copolymer micelles, and nanocrystals (NCs). NCs capped by organic molecules with long alkyl chains, such as oleylamine and/or oleic acid, show a certain degree of "softness" and their crystallization in to superlattice can be regarded as a Kirkwood–Alder transition.[5,6] Because of a tunable repulsion resulting from the deformation of the soft layers, this disorder-to-order transition of NCs experiences a "lyotropic" stage, in which individual NCs are spatially surrounded by solvent molecules while maintaining the superlattice ordering. Although many research efforts have been devoted to investigate the crystallization of "soft particles", most of the studies focused on spherical models with the assumption of isotropic NC interaction potentials.[7−13] Crystallization of nonspherical nanobuilding blocks has attracted attention recently, due to their unusual characteristics of superstructure, packing efficiency and orientational ordering.[13−21]

Self-assembly of nonspherical NCs into ordered supercrystals (SCs) may provide a novel platform on which new materials could be engineered toward various potential applications such as biological sensors and innovative sustainable energy conversion devices. Similar to their molecular analogs, collective properties of SCs as artificial solids are strongly dependent on the coupling between adjacent building blocks, symmetry and lattice spacing in the superstructure.[22] Recently, a substantial research endeavor has also been devoted to shape-controlled synthesis of Pt-based nonspherical NCs from an organic solution system.[23−26] The ability to predict and control the self-assembly of these nonspherical NCs is of both fundamental and practically important. To further understand the mechanism that governs a SC formation as well as the

Received: April 29, 2012
Published: July 27, 2012

dx.doi.org/10.1021/ja304108n | *J. Am. Chem. Soc.* 2012, 134, 14043−14049

relationship between the superstructures and collective properties, a real-time study of a NC Kirkwood−Alder transition with a specific shape of the building blocks is essential.

The successful synthesis of high-quality Pt-based nanoctahedra[23,24,27] enabled us to explore the Kirkwood−Alder transition of Pt_3Cu_2 nanoctahedron building blocks. We have recently reported a *bcc* superstructure consisting of Pt_3Ni nanoctahedra.[27] As is well-known, a conventional *bcc* lattice of spherical particles has a packing efficiency of 68%. Considering the metallic cores only, the peculiar tip-to-tip arrangement found for these nanoctahedra fills only 33% of the super unit cell. In a real assembled SC, however, the building blocks are passivated with a thin layer of organic ligands which fill up more of the available space. In this work, we present our recent observations on the packing structure of SCs containing Pt_3Cu_2 nanoctahedra using transmission electron microscopic (TEM) tomography method as well as their real-time crystallization process driven by a controlled solvent-evaporation using synchrotron-based *in situ* grazing-incidence small-angle X-ray scattering (GISAXS). Investigation results show that the SCs consisting of organic molecule-capped Pt_3Cu_2 nanoctahedra crystallize at a critical concentration and possess continuous crystalline states during a period of solvent evaporation and associated superlattice drying. Such type of a superstructure could be formed independently on the solvent evaporation rate. In addition, the "soft crystal" can be reversely "dissolved", when vapor pressure of the solvent was increased by reducing the inert gas flowing stream through the sample chamber. As a strong contrast to the close-packed face centered cubic (*fcc*) structure predicted for the Kirkwood−Alder transition of hard spheres, the self-assembly of Pt_3Cu_2 nanoctahedra resulted in a non-close-packed body centered cubic (*bcc*) superstructure with a low packing efficiency. At formation, the *bcc* lattice constant is significantly larger than that in the dry assemblies. As discussed in this report (*vide infra*), this can be supported by the observation of an "expended" superstructure with a superlattice parameter of ∼15.3 nm using *in-situ* GISAXS in a controlled solvent vapor environment.

RESULTS AND DISCUSSION

Synthesis and Self-Assembly. The Pt_3Cu_2 nanoctahedra were prepared through a co-reduction of platinum(II) acetylacetonate and a mixture of copper(I)/(II) chloride in the presence of tungsten hexacarbonyl [$W(CO)_6$] in a mixture of oleic acid and oleylamine (1:9 in volume), using a synthetic method developed from the strategy published elsewehere.[23,24,27] A typical preparation procedure and energy dispersive X-ray spectroscopic (EDS) results are detailed in the Supporting Information. ICP-MS composition analysis suggests a molar ratio of ∼60:40 between Pt and Cu. TEM characterization indicates that these Pt_3Cu_2 nanoctahedra have an average side-length of ∼9.6 nm (Figure 1). The oleylamine-capped NCs[23,28] can be regarded as hard cores with soft shells and the shell softness can be calculated as 0.5.[12] An increase of the NC volume fraction induced by solvent evaporation leads to a phase transition from a liquid suspension to a SC with high liquid content predicted by Kirkwood−Alder theory.[5]

Drop-casting of Pt_3Cu_2 nanoctahedron-hexane suspensions onto a TEM grid and drying in ambient condition led to highly ordered assemblies with both monolayer and multilayers as shown in Figure 1a and 1b, respectively. In a monolayer assembly, most of the nanoctahedra were arranged into 2D hexagonal lattices with the [111] orientation. This orientational

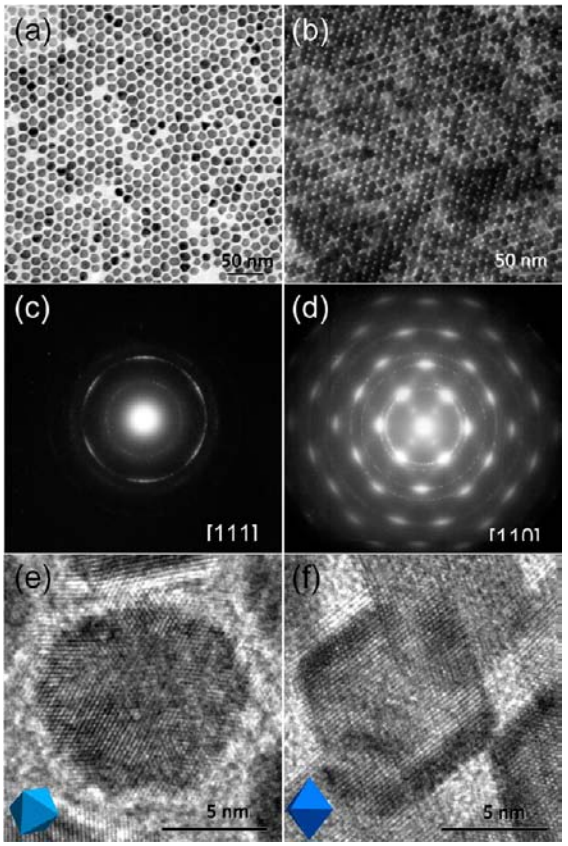

Figure 1. TEM patterns of Pt_3Cu_2 nanoctahedron assemblies. (a and b) monolayer and multilayer assemblies, respectively; (c and d) corresponding electron diffraction patterns to (a) and (b) in projection directions of [111] and [110], respectively; (e and f) high-resolution images of mono- and multilayer assemblies.

ordering was confirmed by a selected-area-electron-diffraction (SEAD) pattern presented in Figure 1c. It is worth noting that the orientation of nanoctahedra in multiple-layer assemblies is different from that in the monolayer. The SAED pattern (Figure 1d) indicates that the majority of the octahedral building blocks in a multiple-layered assembly take the crystal orientation of [110], in contrast to [111] in the monolayer assembly. As additional support, high-resolution TEM images taken from both types of assemblies (Figure 1e and 1f) show two different octahedron orientations.

For a fast drop-casting assembly, one drop of the Pt_3Cu_2 nanoctahedra suspended in hexane was cast on a 200 mesh TEM grid (Ted Pella, 01801) which was preplaced on a piece of filter paper, or on a piece of (111) surface-polished Si wafer under ambient conditions. The number of assembly layers can be tuned by controlling the concentration of the Pt_3Cu_2 suspensions. For a slow "solvent-annealing" refinement, a multilayered SC drop-cast on the same Si wafer was placed into a GISAXS sample chamber (Figure S1) in which the sample was surrounded by additional solvent (hexane) vapor; the solvent evaporation could be controlled by varying the helium flow rate (*vide infra*) through the cell.

Superstructure with a Low Packing Density. Previous investigations already indicated that the superstructure of nonspherical NC assemblies depends on a number of factors including dynamic deposition, ligand-solvent interaction, and geometric shape.[29] For instance, the solvent evaporation rate can significantly affect the NC arrangement in an SC, resulting

dx.doi.org/10.1021/ja304108n | J. Am. Chem. Soc. 2012, 134, 14043−14049

in various superstructures such as body centered tetragonal (*bct*), *fcc*, and *bcc* packings.[13] In this work, we explored the superstructure of Pt_3Cu_2 nanoctahedron SCs prepared through both fast drop-casting and slow controlled solvent-evaporation processes using TEM tomography and GISAXS techniques.

TEM tomography with 3D reconstruction analysis technique was applied to fast drop-cast Pt_3Cu_2 SC on a TEM grid. Figure 2a presents a TEM image with two framed areas enlarged on

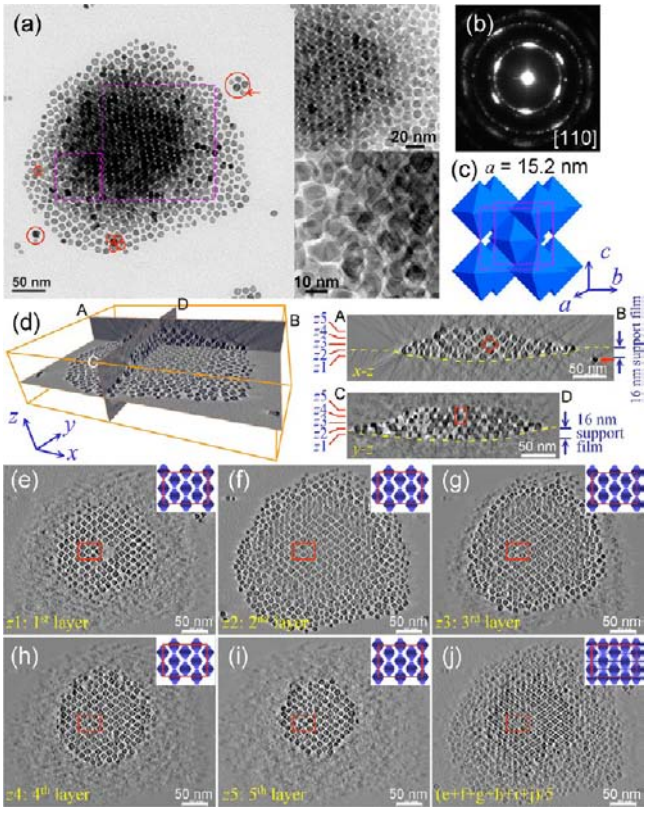

Figure 2. Electron tomographic analysis of superlattice structure. (a) TEM image, with framed areas enlarged on its right side. Circled particles are located underneath the carbon support film; (b) SAED; (c) superlattice model with *bcc* structure; (d) 3D reconstructed volume, with two orthogonal views labeled as AB and CD shown on the right side; (e–i) slice plane views at the heights of $z1$–$z5$ as indicated in (d); (j) averaged intensities of the images (e) through (i). Planar 2 × 2 unit cells are outlined in (e–j), with schematic structural models showing on the top-right corner of each image.

the right panel, where aligned rhombus-shaped NCs are identifiable. Circled particles are identified to be located underneath the carbon support film according to this tomography study. An SAED pattern from this area (Figure 2b) shows a highly textured pattern, indicating that most of the NCs attained the same [110]-crystallographic orientation as the one found for the multilayer pattern (Figure 1d). Figure 2c presents a structural model of a *bcc* superlattice, which is consistent with the superstructure of Pt_3Cu_2 SC in this work. Figure 2d illustrates a 3D reconstructed volume from large tilting angle series (from −62° to 64° at 1° interval), with two orthogonal views shown on the right panel with their top edges marked as AB and CD, respectively. This image indicates that the assembly contained five stacked layers. Along the x–z view ([001] orientation), the NCs form a near squared pattern, whereas both the y–z ([1$\bar{1}$0] orientation)) and the x–y ([110] orientation) views show centered rectangular patterns with an edge ratio close to $\sqrt{2}$:1. Thus, the latter NCs were stacked in a *bcc* lattice (the unit cell is outlined).

It is interesting that the bottom of this agglomerate is not flat but formed a downward depression of the support film, as marked by the broken lines, indicating an effect of gravity, or more likely the surface tension of the agglomerate that tends to favor a spherical shape. The support film is visible in the cross-section views, with a measured thickness of 16 nm that is consistent with the parameter given by the grid vendor. The particle indicated by an arrow under the film is the same one indicated by an arrow in the plane view in Figure 2a. Note that along the z direction, particles are slightly stretched due to a tomography artifact.

A series of representative TEM images were taken at different tilt angles and are shown in Figure S2. A movie of the TEM images during the tilting experiment is also included in Supporting Information (Movie S3). Slice plane views at the height of z1, z2, ..., z5 as marked in Figure 2d are shown in Figure 2e–i, indicating the Pt_3Cu_2 nanoctahedra on the first to fifth layers, respectively. As summarized by a schematic model projection presented in the inset of each corresponding slice-view pattern, the NCs on the same layer formed a near regular, centered rectangular pattern, with 2 × 2 unit cell outlined, and two adjacent layers just offset by half the periodicity along the z direction, suggesting a stacking sequence of AB...AB. Summation of Figure 2e–i, then followed a division by 5, results in an image of white dotted lines (Figure 2j), which has the same image features that were observed in the TEM image (Figure 2a). Superimposing two adjacent model projections produced these observed image features with white dotted lines, which are the empty channels along the viewing direction. The TEM tomography study suggests a *bcc* superstructure in the drop-cast Pt_3Cu_2 SC, with averaged lattice parameters measured as a = 15.2 nm (also see Figure S4).

The "layer-dependent" orientation determination in this octahedral Pt_3Cu_2 system was also observed previously.[27] In most cases, monolayer patterns were packed in [111] orientation. This could be interpreted that a [111]-oriented monolayer pattern can offer the largest contact area between the TEM substrate (film) and the organic ligand-capped particle surface to minimize the total surface energy. However, packing into a *bcc* superlattice along the [111] orientation requires alternatively that half the number of particles among the monolayer hexagonal pattern relocate at a higher level plane which is impossible to occur, since the upper layer would not be supported by the bottom layer. A similar case happens along the [001] orientation, although the upper layer just fills the gap of the bottom-layer square pattern. Along the [011] orientation as shown in the models in Figure 2, however, the upper layer is firmly supported by the bottom layer with large contact areas (or overlapped areas along the z direction), so this stacking is possible to occur as experimentally observed in this work.

To study the formation of the SC, Pt_3Cu_2 nanoctahedron–hexane suspensions were drop-cast onto a polished Si-wafer substrate. The dried film (SC) was studied using the GISAXS technique subsequently. As illustrated in Figure S5a, the yellow marks on the observed GISAXS pattern are the theoretical positions of the diffraction dots of a uniaxially oriented *bcc* 2D powder with the close-packed (110) planes parallel to the substrate. The calculated diffraction pattern matches well with that of a *bcc* structure with a lattice parameter of ~15.3 nm. When refraction is properly accounted for by a matching

dx.doi.org/10.1021/ja304108n | *J. Am. Chem. Soc.* 2012, 134, 14043–14049

incident and critical angle with the corresponding scattering features,[10,30] we determined only a slight compression of 2% or less of the lattice perpendicular to the (110) plane due to drying forces.

Both the TEM tomography and GISAXS studies suggest an almost perfect *bcc* superstructure with high degree of translational and orientational ordering in an SC containing Pt_3Cu_2 nanoctahedra. The theoretical volume fraction of such SCs can be determined as 33.3% based on the perfect octahedral shaped Pt_3Cu_2 NCs, as we found in a previous study on Pt_3Ni nanoctahedra,[27] which however lacked the detailed examination of the SC formation as discussed in the following section.

Previous studies have revealed that the crystallography of self-assembled SCs can be strongly affected by the geometrical shape of their building blocks.[27,29,31,32] Glotzer and co-workers predicted a *bcc* packing for hard nanoctahedra in their recent Monte Carlo simulations.[21] However, they did not find the tip-to-tip alignment of adjacent NCs.[21] The particular arrangement may have been mediated by ligand−ligand interactions based on an anisotropic ligand distribution on the nanoctahedron surface which were not included in their simulation.[13,33] In particular, at vertices and edges of the faceted cores, ligands are in a highly frustrated conformation. Ligand shell effects promoting the formation of non-close-packed lattices were conjectured by Goodfellow and Korgel in their recent perspective,[34] in which they pointed out the close analogy between NC assemblies and ordered, close-packed block copolymer micelles.[11] Recently, Hennig and collaborators also provided further theoretical evidence to support such a mechanism.[35]

Softness. In a colloidal solution, NCs can be considered as artificial atoms, or "soft spheres".[36] A formation of SCs from the colloidal solution can be regarded as crystallization. Despite many studies of Kirkwood−Alder transition of sphere-like particles, little is known about the crystallization process involving *nonspherical* colloidal NCs. Using GISAXS in combination with a special solvent vapor treatment chamber, as illustrated in Supporting Information (refer to Figure S1), *in-situ* continuous superstructural changes during an assembly process of Pt_3Cu_2 nanoctahedra were observed.

The GISAXS patterns were recorded at a predefined interval of time, while a drop of Pt_3Cu_2 nanoctahedron−hexane suspension deposited on a silicon wafer was slowly dried up under a faint stream of helium gas flowing through the sample chamber with a controlled flow rate. Once a drop of Pt_3Cu_2 nanoctahedron−hexane suspensions was deposited on the substrate, the diffraction pattern showed a broad intensity distribution but no distinct dots, indicating a homogeneous colloidal solution with liquid-like disorder. As the sample was slowly drying, discrete Bragg spots started to gradually appear in the patterns gradually, implying the formation of ordered structures. Figure 3 shows some critical 2D patterns with the time evolution. A movie of GISAXS patterns during Pt_3Cu_2 nanoctahedron self-assembly as a function of time is included in the Supporting Information (Movie S6), showing a continuous change of diffraction spot positions while the SC is slowly drying.

On the basis of various theoretical and experimental studies, colloids start to self-assemble into ordered structures once the volume fraction of a colloidal suspension reaches a threshold value.[10,37,38] As the solvent evaporation proceeded, the diffraction spots of the patterns continuously shifted away

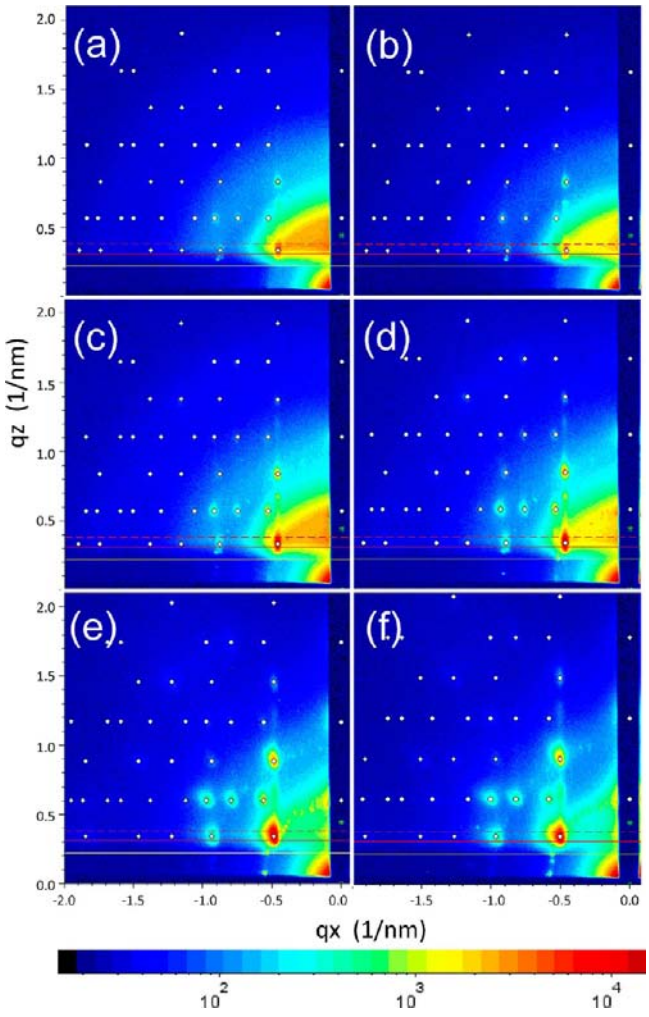

Figure 3. Selected GISAXS patterns of Pt_3Cu_2 nanoctahedron self-assembly as a function of the solvent evaporation time. Frame numbers (a−f) correspond to the rows in Table 1. Spot positions were fitted (circles) and the radial spot widths were determined. The yellow, solid red, and dashed red lines indicate the sample horizon, and the critical angles of the film, and the substrate, respectively. At the early stages of drying (a−c), the form factor scattering of the concentrated solution is superimposed to the sharp spots of the condensing supercrystal. The *bcc* structure of the superlattice was maintained during the drying, while the broadening of the diffraction spots indicates a degradation of the grain size. The time evolution of lattice parameters and grain sizes are listed in Table 1.

from the origin. Eventually, the diffraction spots stabilized at a fixed position when the specimen pattern was completely dried which corresponds to a *bcc* structure (refer to Figure S5a). As commonly known for an ordered SC pattern, the position shift of the diffraction spots correlates to the shrinkage of the superlattice parameters of such an ordered structure.[6] As presented in Table 1, fitting these diffraction patterns reveals a range of lattice constants between 16.7 and 15.3 nm of this *bcc* SC. If we assume that the final lattice constant of a_f = 15.3 nm refers to the completely dried superlattice, we can estimate the critical NC concentration at which the SC forms from the first discernible crystallization at a_i = 16.7 nm to be given by $(a_f/a_i)^3$ = 76.9%. This value is close to the Kirkwood−Alder value of 73.6% for the ratio of transition density and densest packing in noninteracting hard spheres.[5]

dx.doi.org/10.1021/ja304108n | J. Am. Chem. Soc. 2012, 134, 14043−14049

Table 1. Calculated Lattice Parameter and Grain Size Corresponding to Each GISAXS Frame in Figure 3

frame number	time (min)	calculated lattice parameter (nm)	calculated grain size (nm)
a	11	16.7	154
b	16	16.5	165
c	21	16.5	149
d	32	16.2	114
e	41	16.0	75
f	60	15.3	71

Such a continuous change of the SC lattice parameter can be visualized by a comparison using azimuthally integrated GISAXS intensity profiles as shown in Figure 4a. Initially, only broad form factor oscillations are shown due to scattering from the concentrated solution. At the onset of the Kirkwood–Alder transition, sharper superlattice Bragg reflections appeared. During this transition stage, the initially formed superstructure is similar to the final *bcc* SC structure, but with a larger lattice constant. In this initial structure, the nanoctahedra did not form a mechanical close-contact with each other. It is believed that the building blocks are surrounded by a shell of solvent molecules embedded between the ligand coronae. Even though these nanoctahedra still form a *bcc* arrangement, the transition is classified as a Kirkwood–Alder transition.[5] As drying proceeded, the Bragg reflections shifted outward and broadened somewhat. The broadening indicates that some disorder appears in the superlattices as the solvent leaves the lattice, leading to a reduced grain size. A detailed analysis[39] showed that the grain size was essentially isotropic with regard to the lateral and perpendicular direction. When superlattices condensed from solution, the grain size was about 160 nm. However, in the late stages of drying, the grain size was reduced by more than 50% to about 70 nm, indicating a large amount of grain breakage, as the solvent left the lattice. Results are listed in Table 1.

The attractive interaction between NCs is provided by the van der Waals forces, in addition to dipole moment, magnetic, and other possible forces if existing, whereas the repulsive forces that stop NC-aggregation are mainly from steric interactions due to the "tail-repulsion" of the organic capping ligands. The final structure of a NC assembly will depend on a "balance" between such attractive and repulsive interactions.[38]

Reversibility. One of the most intriguing features observed on the Pt_3Cu_2 SC system is the reversibility of the order–disorder transition. As discussed above, the lattice parameter of a Pt_3Cu_2 nanoctahedron system varies between a larger value at the order–disorder transition and a smaller one for the completely dried SC during an assembly process. Furthermore, we have determined that the lattice parameter experiences an expansion when an ensemble of dried SC was "liquefied", that is, the solvent content in the structure was increased to an extent that the superlattice lost its long-range *bcc* order and regained the liquid-like structural factor corresponding to a concentrated solution. In addition, the superlattices were uniaxially oriented due to the presence of a substrate, as they underwent assembly and disassembly facilitating these detailed studies. In an early study, Connolly et al. reported structural formation during the drying of spherical silver nanoparticles using time-resolved SAXS measurements of nanoparticle

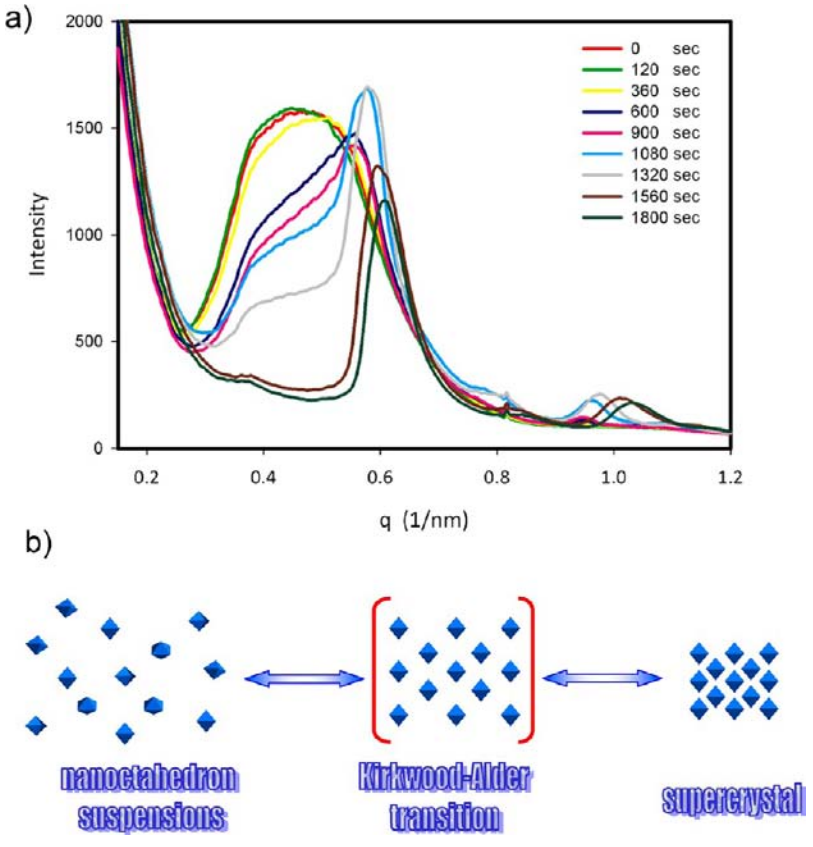

Figure 4. (a) Series of azimuthally integrated GISAXS intensity profiles, recorded versus solvent evaporation time, showing the gradual lattice shrinkage; (b) schematic showing the lattice change during crystallization.

dx.doi.org/10.1021/ja304108n | J. Am. Chem. Soc. 2012, 134, 14043–14049

suspensions.[40] In this study, an exquisite vapor pressure control was used to select the speed of assembly and disassembly to transit from concentrated solution to highly ordered superlattices and back.

As demonstrated in Figure 4a, the scattering vector, q, continuously decreased when a piece of dried SC was gradually saturated with a hexane vapor using the same vapor chamber, a process also known as "solvent annealing". Since the characteristic q is inversely proportional to the lattice spacing of a SC, Figure 4a implies that such a *bcc*-structured SC can be reversely disassembled. The presence of such a reversible transition state could also provide an opportunity of improving the quality of SCs.[10] For instance, as shown in Figures S5b,c, the size and quality patterned SCs being treated via a solvent vapor treatment and successive controlled drying process is much better than that prepared via a simple drop-casting method.

In a dried SC in which NCs are packed in their respective lattice sites with low mobility, it is impossible to remove defects such as vacancies, interstitials, or dislocations that may form in a SC due to the fast "crystallization" process during drop-casting.[10] One way to minimize those defects is to "extend" the duration of the transition state during the assembly process by judiciously controlling the vapor pressure in the chamber. In this case, these NC building blocks could be rearranged toward a highly ordered structure. A schematic model concerning this solvent evaporation/drying process is proposed in Figure 4b. As shown in Figure 5, the evolution of 1D GISAXS patterns of an

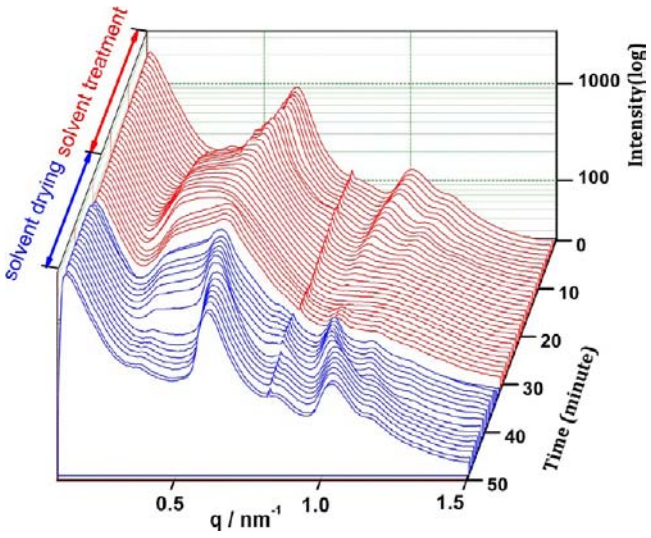

Figure 5. Evolution of azimuthally integrated GISAXS patterns of a film of Pt_3Cu_2 nanoctahedra during controlled drying and solvent vapor treatment. The *in situ* and real-time data show the reversibility of lattice change during the formation and dissolution of supercrystals.

SC consisting of Pt_3Cu_2 nanoctahedra during solvent drying and solvent vapor treatment further demonstrates a reversibility of the lattice change corresponding to a formation and dissolving of SCs. On the basis of our experimental evidence, the formation mechanism of the observed SCs consisting of Pt_3Cu_2 nanoctahedra, which was identified as a Kirkwood–Alder transition, is quite consistent with a recent finding of a theoretical study on the packing of nanoctahedra.[21]

CONCLUSIONS

A peculiar open *bcc* superstructure with a tip-to-tip arrangement of adjacent nanoctahedra has been determined as the only structure to form in drop-cast SCs consisting of Pt_3Cu_2 nanoctahedra using both TEM tomography and GISAXS techniques. *In-situ* GISAXS was used to monitor the structural changes via solvent vapor treatment and slow drying. In this way, we found the nanoctahedra crystallized readily at a high solvent content with a significantly larger lattice constant than dry deposits, thus, classifying the crystallization as a soft Kirkwood–Alder transition. During the controlled solvent annealing and evaporation/drying processes, the resulting SCs composed of Pt_3Cu_2 nanoctahedra remained in their initial *bcc* structure, demonstrating a reversible shrinkage/expanding of the lattice that is uniform despite the nonspherical shape of the building blocks. This feature of superstructure reversibility in the current system was, for the first time, observed experimentally. Together with soft assembly and low packing efficiency, this characteristic enables prospective development of "smart", environmentally adaptable materials for potential applications in sensors and catalysts.

ASSOCIATED CONTENT

Supporting Information

Synthesis procedure of Pt_3Cu_2 nanoctahedra, characterization methods, EDS composition analysis results, schematic of experimental setup for GISAXS, representative TEM images taken at different tilting angles, movie of TEM image during the tilting experiment, electron tomographic structure (high resolution), GISAXS pattern and SEM image of drop-cast Pt_3Cu_2 nanoctahedron supercrystal, movie of Pt_3Cu_2 nanoctahedron self-assembly via GISAXS patterns taken during slow drying, and a large-area SEM image of Pt_3Cu_2 supercrystal. This material is available free of charge via the Internet at http://pubs.acs.org.

AUTHOR INFORMATION

Corresponding Author

*jfang@binghamton.edu; dms79@cornell.edu

Present Addresses

[#]Center for Nanoscale Materials, Argonne National Laboratory, Argonne, Illinois 60439, USA

[¶]Department of Chemistry and Physics, Fayetteville State University, Fayetteville, NC 28301, USA

Notes

The authors declare no competing financial interest.

ACKNOWLEDGMENTS

We thank Dr. Kaikun Yang and Prof. Howard Wang from the Department of Mechanical Engineering, as well as Dr. Hongzhou Yang and Prof. Shouzhong Zou from the Department of Chemistry and Biochemistry, Miami University, for their contributions and technical help in the SEM observations and ICP-MS determination, respectively. This work was partially supported by NSF (DMR-0731382) and the S^3IP center at SUNY Binghamton. Part of this work was conducted at the Cornell High Energy Synchrotron Source (CHESS) which is supported by the National Science Foundation and the National Institutes of Health/National Institute of General Medical Sciences under NSF award DMR-0936384.

REFERENCES

(1) Kirkwood, J. G. *J. Chem. Phys.* **1939**, *7*, 919−925.
(2) Alder, B. J.; Wainwright, T. E. *J. Chem. Phys.* **1957**, *27*, 1208−1209.
(3) Alder, B. J.; Wainwright, T. E. *Phys. Rev.* **1962**, *127*, 359−361.
(4) Alder, B. J.; Hoover, W. G.; Young, D. A. *J. Chem. Phys.* **1968**, *49*, 3688−3696.
(5) Gast, A. P.; Russel, W. B. *Phys. Today* **1998**, *51*, 24−30.
(6) Cheng, W.; Hartman, M. R.; Smilgies, D.-M.; Long, R.; Campolongo, M. J.; Li, R.; Sekar, K.; Hui, C.-Y.; Luo, D. *Angew. Chem., Int. Ed.* **2010**, *49*, 380−384.
(7) Macfarlane, R. J.; Lee, B.; Jones, M. R.; Harris, N.; Schatz, G. C.; Mirkin, C. A. *Science* **2011**, *334*, 204−208.
(8) Macfarlane, R. J.; Lee, B.; Hill, H. D.; Senesi, A. J.; Seifert, S.; Mirkin, C. A. *Proc. Natl. Acad. Sci. U.S.A.* **2009**, *106*, 10493−10498.
(9) Cheng, W.; Campolongo, M. J.; Cha, J. J.; Tan, S. J.; Umbach, C. C.; Muller, D. A.; Luo, D. *Nat. Mater.* **2009**, *8*, 519−525.
(10) Hanrath, T.; Choi, J. J.; Smilgies, D.-M. *ACS Nano* **2009**, *3*, 2975−2988.
(11) McConnell, G. A.; Gast, A. P.; Huang, J. S.; Smith, S. D. *Phys. Rev. Lett.* **1993**, *71*, 2102−2105.
(12) Chen, Z.; Moore, J.; Radtke, G.; Sirringhaus, H.; O'Brien, S. *J. Am. Chem. Soc.* **2007**, *129*, 15702−15709.
(13) Choi, J. J.; Bealing, C. R.; Bian, K.; Hughes, K. J.; Zhang, W.; Smilgies, D.-M.; Hennig, R. G.; Engstrom, J. R.; Hanrath, T. *J. Am. Chem. Soc.* **2011**, *133*, 3131−3138.
(14) Wang, Z. L.; Harfenist, S. A.; Vezmar, I.; Whetten, R. L.; Bentley, J.; Evans, N. D.; Alexander, K. B. *Adv. Mater.* **1998**, *10*, 808−812.
(15) Zheng, R.; Gu, H.; Xu, B.; Fung, K. K.; Zhang, X.; Ringer, S. P. *Adv. Mater.* **2006**, *18*, 2418−2421.
(16) Zhang, J.; Kumbhar, A.; He, J.; Das, N. C.; Yang, K.; Wang, J.-Q.; Wang, H.; Stokes, K. L.; Fang, J. *J. Am. Chem. Soc.* **2008**, *130*, 15203−15209.
(17) Lu, W.; Liu, Q.; Sun, Z.; He, J.; Ezeolu, C.; Fang, J. *J. Am. Chem. Soc.* **2008**, *130*, 6983−6991.
(18) Chen, M.; Kim, J.; Liu, J. P.; Fan, H.; Sun, S. *J. Am. Chem. Soc.* **2006**, *128*, 7132−7133.
(19) Disch, S.; Wetterskog, E.; Hermann, R. P.; Salazar-Alvarez, G.; Busch, P.; Bruckel, T.; Bergström, L.; Kamali, S. *Nano Lett.* **2011**, *11*, 1651−1656.
(20) Henzie, J.; Grünwald, M.; Widmer-Cooper, A.; Geissler, P. L.; Yang, P. *Nat. Mater.* **2012**, *11*, 131−137.
(21) Damasceno, P. F.; Engel, M.; Glotzer, S. C. *ACS Nano* **2012**, *6*, 609−614.
(22) Zhang, Y.; Lu, F.; Lelie, D. v. d.; Gang, O. *Phys. Rev. Lett.* **2011**, *107*, 135701.
(23) Zhang, J.; Fang, J. *J. Am. Chem. Soc.* **2009**, *131*, 18543−18547.
(24) Zhang, J.; Yang, H.; Fang, J.; Zou, S. *Nano Lett.* **2010**, *10*, 638−644.
(25) Wang, C.; Daimon, H.; Lee, Y.; Kim, J.; Sun, S. *J. Am. Chem. Soc.* **2007**, *129*, 6974−6975.
(26) Xu, D.; Liu, Z.; Yang, H.; Liu, Q.; Zhang, J.; Fang, J.; Zou, S.; Sun, K. *Angew. Chem., Int. Ed.* **2009**, *48*, 4217−4221.
(27) Zhang, J.; Luo, Z.; Quan, Z.; Wang, Y; Kumbhar, A.; Smilgies, D.-M.; Fang, J. *Nano Lett.* **2011**, *11*, 2912−2918.
(28) Zhang, J.; Yang, H.; Yang, K.; Fang, J.; Zou, S.; Luo, Z.; Wang, H.; Bae, I.-T.; Jung, D. Y. *Adv. Funct. Mater.* **2010**, *20*, 3727−3733.
(29) Quan, Z.; Fang, J. *NanoToday* **2010**, *5*, 390−411.
(30) Smith, D. K.; Goodfellow, B.; Smilgies, D.-M.; Korgel, B. A. *J. Am. Chem. Soc.* **2009**, *131*, 3281−3290.
(31) Wang, Z. L. *Adv. Mater.* **1998**, *10*, 13−30.
(32) Gang, O.; Zhang, Y. *ACS Nano* **2011**, *5*, 8459−8465.
(33) Bian, K.; Choi, J. J.; Kaushik, A.; Clancy, P.; Smilgies, D.-M.; Hanrath, T. *ACS Nano* **2011**, *5*, 2815−2823.
(34) Goodfellow, B. W.; Korgel, B. A. *ACS Nano* **2011**, *5*, 2419−2424.
(35) Bealing, C. R.; Baumgardner, J.; Choi, J. J.; Hamrath, T.; Hennig, R. G. *ACS Nano* **2012**, *6*, 2118−2127.
(36) Korgel, B. A.; Fullam, S.; Connolly, S.; Fitzmaurice, D. *J. Phys. Chem. B* **1998**, *102*, 8379−8388.
(37) Koh, Y. K.; Wong, C. C. *Langmuir* **2006**, *22*, 897−900.
(38) Bishop, K. J. M.; Wilmer, C. E.; Soh, S.; Grzybowski, B. A. *Small* **2009**, *5*, 1600−1630.
(39) Smilgies, D.-M. *J. Appl. Crystallogr.* **2009**, *42*, 1030−1034.
(40) Connolly, S.; Fullam, S.; Korgel, B.; Fitzmaurice, D. *J. Am. Chem. Soc.* **1998**, *120*, 2969−2970.